JGR Space Physics

RESEARCH ARTICLE
10.1029/2021JA030250

Key Points:

- Six hundred and fifty five nights with equatorial plasma bubbles (EPBs) occurrence were analyzed using detrended total electron content (dTEC) at geomagnetically conjugate points over the Brazilian sector
- In ~30% of the nights the EPBs presented an apparent inter-hemispheric asymmetry
- Meridional wind data and numerical simulation results suggested that the inter-hemispheric asymmetry is due to a trans-equatorial meridional wind

Correspondence to:
D. Barros,
diego.barros@inpe.br

Citation:
Barros, D., Takahashi, H., Wrasse, C. M., Carrasco, A. J., Figueiredo, C. A. O. B., & Inoue Junior, M. H. (2022). Asymmetric development of equatorial plasma bubbles observed at geomagnetically conjugate points over the Brazilian sector. *Journal of Geophysical Research: Space Physics*, *127*, e2021JA030250. https://doi.org/10.1029/2021JA030250

Received 5 JAN 2022
Accepted 21 MAY 2022

Asymmetric Development of Equatorial Plasma Bubbles Observed at Geomagnetically Conjugate Points Over the Brazilian Sector

D. Barros[1], H. Takahashi[1], C. M. Wrasse[1], A. J. Carrasco[2], C. A. O. B. Figueiredo[1], and M. H. Inoue Junior[1]

[1]Instituto Nacional de Pesquisas Espaciais, São José dos Campos, Brazil, [2]Universidad de los Andes, Mérida, Venezuela

Abstract Ground-based global navigation satellite systems (GNSS) receivers have been used to monitor the meridional (north-south) development of equatorial plasma bubbles (EPBs) at geomagnetically conjugate points over the Brazilian sector. EPBs were studied using detrended total electron content plots obtained from Boa Vista (MLat: 9.6°N), Itacoatiara (MLat: 3.3°N), Colíder (MLat: 5.0°S), and Cuiabá (MLat: 8.8°S) GNSS receivers. All GNSS receivers are located approximately under the same magnetic meridian. 655 nights with EPBs occurrence were analyzed using data from January 2012 to February 2016. In 459 nights (~70%) the EPBs presented a symmetric development with respect to the geomagnetic equator. However, in 196 nights (~30%) the EPBs presented an apparent asymmetry. The asymmetries are characterized as a displacement of the EPBs to north (or south) of the geomagnetic equator. The highest north (south) asymmetry occurrence was observed during December to January (March to April and September to October), and lowest during March to April and August to September (December to January). To investigate these asymmetries, we analyzed meridional wind data and used a numerical model to simulate the EPBs evolution. Both meridional wind data and numerical simulation results suggested that a trans-equatorial meridional wind blowing to north (south) would be able to cause a displacement of the EPBs to north (south) of the geomagnetic equator.

1. Introduction

Equatorial plasma bubbles (EPBs) are large-scale irregularities that occur during nighttime in the F region of the equatorial ionosphere (for example, Abdu, Batista, et al., 2009; Huang et al., 2013; Pimenta et al., 2003; Sahai et al., 1994; Sobral et al., 1981; Tsunoda & Livingston, 1982). Equatorial plasma bubbles are characterized as a decrease of the ionospheric plasma density. Around the sunset time, the pre-reversal enhancement of the electric field (PRE) (Rishbeth, 2000) causes a rapid uplift of the equatorial F-layer, originating in its bottom-side a large density gradient. Under this condition, the F region bottom-side becomes unstable and EPBs can be generated by the Rayleigh–Taylor instability (RTI) (Haerendel, 1973; Kelley, 2009). However, the RTI needs a perturbation such as atmospheric gravity waves (GWs) (Abdu, Kherani, et al., 2009; Fagundes et al., 1995; Hysell et al., 1990; Woodman & LaHoz, 1976) or large-scale wave structures (LSWSs) (Thampi et al., 2009; Tsunoda, 2006; Tulasi Ram et al., 2012, 2014) to be initiated.

The general features of EPBs have been extensively investigated using both ground- and space-based observations (Abdu et al., 1983, 1991, 2003, 2012; Abdu, Batista, et al., 2009; Abdu, Kherani, et al., 2009; Arruda et al., 2006; De Rezende et al., 2007; Huang et al., 2002, 2013; Magdaleno et al., 2017; Makela et al., 2004; Maruyama, 1984; McNamara et al., 2013; Muralikrishna et al., 2007; Park et al., 2015; Paulino et al., 2011; Pimenta et al., 2003; Takahashi et al., 2014, 2015, 2016, 2018; Tsunoda, 1981). However, only a limited number of studies have been carried out regarding to EPBs meridional (north-south) development observations. Using OI630 nm airglow all-sky imagers at geomagnetically conjugate sites, Otsuka, Shiokawa et al. (2002) showed that EPBs are highly symmetric with respect to the geomagnetic equator. The observations were conducted at Sata (31°N, 130.7°E; MLat: 24°N), Japan, and Darwin (12.4°S, 131°E; MLat: 22°S), Australia, which allowed them to investigate fossil EPBs. Sobral et al. (2009) studied the evolution and developed stages of EPBs using geomagnetically conjugate observations during the conjugate point equatorial experiment (COPEX) campaign (Abdu, Batista, et al., 2009). They used OI630 nm airglow all-sky imagers at Boa Vista (2.8°N, 60.7°W; MLat: 9.6°N) and Campo Grande (20.5°S, 54.7°W; MLat: 13.6°S). The authors showed that EPBs were symmetric and aligned with the geomagnetic field lines, indicating that the zonal (west-east) wind effect during the eastward motion of the

plasma is an integrated effect along the flux tube. Since the polarization electric field produced inside the EPBs maps simultaneously to both hemispheres along the geomagnetic field lines (Mendillo & Baumgardner, 1982; Kelley, 2009), we should expect highly symmetric EPBs. On the other hand, Su et al. (2006) and Sidorova (2021) using ISS-b (~972–1220 km altitude), ROCSAT-1 (~600 km altitude), and AE-E (~300–475 km altitude) satellites data analyzed the latitudinal distributions of the EPBs during periods of moderate to high solar activity. Both studies reported a clear inter-hemispheric asymmetry during equinoxes and solstices periods. In addition to that, Sau et al. (2017) showed an asymmetric EPB using OI630 nm airglow all-sky images at Tirunelveli (8.7°N, 77.8°E; MLat: 1.7°N) and Kolhapur (16.7°N, 74.3°E; MLat: 11.5°N) on Saint Patrick's Day geomagnetic storm of 2015 (17 March). The asymmetry was related to a decay in the polarization electric field within the EPB. However, the authors focused on small structures such as bifurcation (Shiokawa et al., 2004; Yokoyama et al., 2014) within the EPB.

In this paper, we report EPBs meridional (north-south) development observations using detrended total electron content (dTEC) plots over the Brazilian sector. Four global navigation satellite systems (GNSS) receivers located along the same magnetic meridian were used to calculate the dTEC plots. 655 nights with EPBs occurrence were analyzed. On some nights, EPBs presented an apparent asymmetry with respect to the geomagnetic equator. Therefore, we present the general characteristics of these asymmetries and discussions about possible causes.

2. Observations

Each global positioning system (GPS) satellite at an altitude of 20,200 km transmits a dual-frequency radio signals (f_1 = 1575.42 MHz and f_2 = 1227.60 MHz), which allow us to calculate the slant TEC (STEC). The STEC is the number of electrons integrated between GPS satellite and the ground-based dual-frequency GNSS receiver along a column of 1 m squared cross section. Each satellite transmits a pseudorandom noise (PRN) for its identification. Each frequency (f_1 and f_2) provides both phase delay ($\Phi_{1,2}$) and pseudo-range ($P_{1,2}$). $\Phi_{1,2}$ and $P_{1,2}$ are proportional to STEC. A nanosecond delay corresponds to 2.852 TEC units (TECU) and a TECU corresponds to 1×10^{16} electrons/m^2. The relative STEC (STEC$_R$) can be obtained from the STEC calculated using both phase delay (STEC$_\Phi$) and pseudo-range (STEC$_P$) as follows.

$$STEC_R = STEC_\Phi + \langle STEC_P - STEC_\Phi \rangle. \tag{1}$$

Where:

$$STEC_p = \frac{1}{40.3}\frac{f_1^2 f_2^2}{f_1^2 - f_2^2}\left[(P_2 - P_1) - b^P_{1r,2r} - b^P_{1s,2s} - m^P_{1,2} - \xi^P_{1,2}\right], \tag{2}$$

$$STEC_\Phi = \frac{1}{40.3}\frac{f_1^2 f_2^2}{f_1^2 - f_2^2}\left[(\Phi_2 - \Phi_1) - (\lambda_1 N_1 - \lambda_2 N_2) - b^\Phi_{1r,2r} - b^\Phi_{1s,2s} - m^\Phi_{1,2} - \xi^\Phi_{1,2}\right]. \tag{3}$$

In Equations 2 and 3, $b_{1,2}$, $m_{1,2}$, $\xi_{1,2}$, $\lambda_{1,2}$, and $N_{1,2}$ are the hardware delays, the error due to multipath, the error due to noise, the phase wavelength, and phase ambiguities, respectively (Coco et al., 1991; Dear & Mitchell, 2006; Mannucci et al., 1998; Otsuka, Ogawa, et al., 2002; Sardon & Zarraoa, 1997). The vertical component of STEC$_R$ (TEC$_R$) is calculated by multiplying the STEC$_R$ by a slant factor (S), that is, TEC$_R$ = S × STEC$_R$. S is the ratio between the path length of the ray signal within the ionosphere and the thickness of the ionosphere. The TEC$_R$ error increases with the slant factor. Therefore, only GPS satellite elevation angles greater than 30° are computed in TEC$_R$ (Barros et al., 2018; Otsuka, Ogawa, et al., 2002; Takahashi et al., 2016). The TEC$_R$ is calculated for each pair GPS satellite-GNSS receiver with a sampling interval of 30 s.

2.1. EPBs Detection

Equatorial plasma bubbles cause severe scattering and diffraction on GNSS signal, resulting in rapid random fluctuation in TEC$_R$ (Basu et al., 1999; de Jesus et al., 2020; Doherty et al., 1994). These rapid random fluctuations can be used to detect EPBs signature by calculating the dTEC. The dTEC is calculated subtracting the $\overline{TEC}_R$ trend (1 hr running average) from the TEC$_R$(t) (Figueiredo, Wrasse, et al., 2017; Figueiredo et al., 2018; Tsugawa et al., 2006, 2007) as follows.

$$dTEC(t) = TEC_R(t) - \overline{TEC}_R(t \pm 30\text{min}). \quad (4)$$

In this work, EPBs are defined as a dTEC oscillations with amplitudes larger than ±1 TECU. The threshold of ±1 TECU was chosen to avoid the influence of other disturbances such as medium- and large-scale traveling ionospheric disturbances. Similar methodology has been described by Haase et al. (2011), Takahashi et al. (2015, 2018, 2021), Li et al. (2020), and Tang et al. (2020). Figure 1 shows examples of nights with (a and b) and without (c and d) EPBs occurrence.

Figure 1a presents the EPBs occurrence on the night of January 16 to 17, 2015. TEC Maps (upper panel), OI630 nm unwarped images (second panel), ionograms (third panel), dTEC GPS tracks (forth panel), and dTEC time series (bottom panel) are presented. The geographic and geomagnetic coordinates of the instrumentation used in this work are listed in Table 1. The geomagnetic coordinates were obtained by International Geomagnetic Reference Field 2012 (IGRF12) (Thébault et al., 2015).

TEC Maps, OI630 nm images, and ionograms are for the times around 23:10 UT (Universal Time = Local Time + 3h, at 45° W), 00:50 UT, 01:40 UT, and 05:10 UT. OI630 nm images and ionograms were measured by an all-sky imager and a Digisonde Portable Sounder-4 (DPS4), respectively. Both instruments are localized at Boa Vista (BV). In the TEC Maps, the vertical low TEC belts (black arrows) are most likely EPBs signatures (Barros et al., 2018; Takahashi et al., 2014, 2016, 2018). Same EPBs signatures can be seen in the BV OI630 nm images and BV ionograms as a dark bands (Otsuka, Shiokawa, et al., 2002; Sobral et al., 2009; Takahashi et al., 2015; Wrasse et al., 2021) (red arrows) and a spread-F (Abdu, 2016; Agyei-Yeboah et al., 2021; Tulasi Ram et al., 2008) (red arrows), respectively. The dTEC GPS tracks are for the PRNs 14, 23, 31, and 32 at sub-ionospheric point (SIP). The SIP indicates the place where the signal of the GPS satellite crosses the ionospheric F-layer at an altitude of 350 km (Haase et al., 2011). The color shades indicate the amplitude of dTEC oscillations. The green arrows indicate the absence of EPBs and the red arrows indicate the presence of EPBs. The dTEC time series is the period from 20:00 UT to 09:00 UT. It was considered all PRNs (26 PRNs) inside the BV OI630 nm field of view.

At 23:10 UT, no EPB occurrence is seen near BV in the TEC Map, BV OI630 nm images, BV ionograms, and dTEC. On the other hand, at 00:50 UT, 01:40 UT, and 05:10 UT we can clearly see the presence of EPB in the BV OI630 nm images, BV ionograms, and dTEC. The dTEC is able to detect EPB occurrence from the onset time until their disappearance and a wide spectrum of EPB scale size. Large dTEC fluctuations indicate strong EPB growth (at 00:50 UT and 01:40 UT), while small dTEC fluctuations indicate weak EPB (at 05:10 UT). Moreover, dTEC shows a good agreement with EPBs time occurrence reported in the literature, starting around sunset time and lasting several hours (de Jesus et al., 2020; Makela et al., 2004). The dTEC GPS tracks also seemed to agree with BV OI630 nm images about EPB localization.

Although the TEC Maps clearly show the presence of EPBs in the southern part of Brazil, no EPB can be seen in the TEC Maps near BV. TEC Maps are based on GNSS receivers' distribution. The majority of GNSS receivers is located in the southern part of Brazil. The GNSS receivers' distribution in the northern part of Brazil, especially in the Amazon region, are very few. In order to compensate for the lack of data, TEC is smoothed temporally. In general, the spatial resolution is ∼50 km in the southern part of Brazil and larger than 500 km in the northern part (Takahashi et al., 2016). TEC Maps' spatial resolution does not allow us to identify the EPBs occurrence in the northern part of Brazil, especially in the northern side of geomagnetic equator.

Figure 1b presents the comparison between TEC Maps, BV OI630 nm images, BV ionograms, dTEC GPS tracks, and dTEC time series on the night of January 17 to 18, 2015. It clearly shows the EPBs occurrence at 00:00 UT, 02:40 UT, and 03:40 UT. Figure 1c and 1d are typical examples of nights with no EPB occurrence. Note that the dTEC time series presented small oscillations that may be associated to other disturbances (Figueiredo et al., 2018; Takahashi et al., 2018, 2021), but no oscillation was larger than ±1 TECU. The good agreement between TEC Maps, BV OI630 nm images, BV ionograms, and dTEC confirms that the dTEC is able to monitor the EPBs in high spatial and temporal resolution.

2.2. dTEC Analysis

Four GNSS receivers have been used to calculate dTEC and then monitor the EPBs meridional development along the same magnetic meridian. The GNSS receivers are located at Boa Vista (BOAV), Itacoatiara (ITAM),

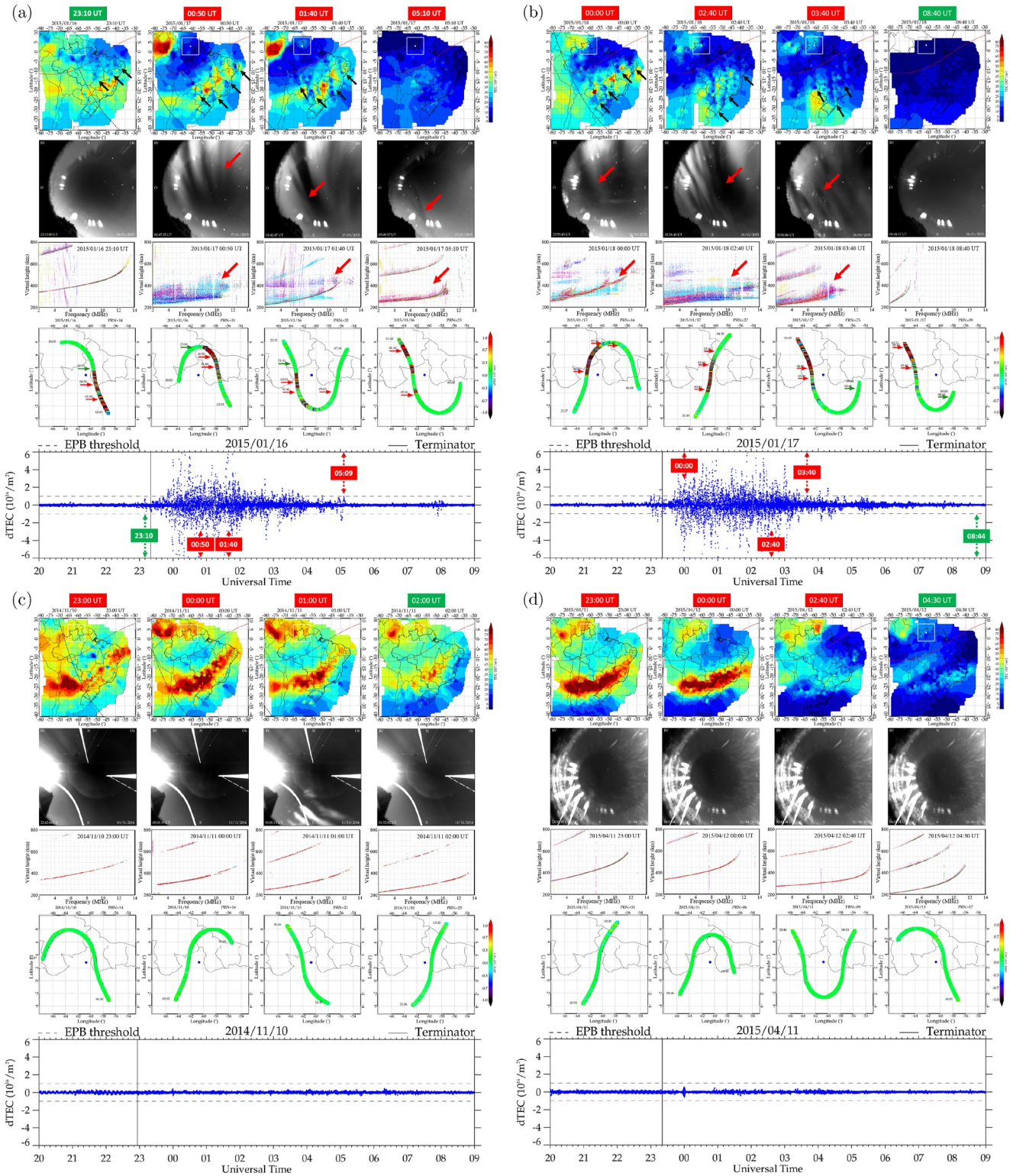

Figure 1. Examples of nights with (a–b) and without (c–d) equatorial plasma bubbles (EPBs) occurrence. In the total electron content (TEC) Maps, the red line, dashed black line, white dot, and the white box represent the geomagnetic equator (at 350 km altitude), solar terminator (at 350 km altitude), Boa Vista (BV) all-sky imager localization, and BV all-sky imager field of view, respectively. The black (TEC Maps) and red arrows (BV OI630 nm images, BV ionograms, detrended total electron content (dTEC) global positioning system (GPS) tracks, and dTEC time series) indicate EPBs signatures. The green arrows (dTEC GPS tracks and dTEC time series) indicate no EPB occurrence. In the dTEC GPS tracks, the start and end time of the observations are marked near the GPS satellite tracks.

Table 1
Geographic and Geomagnetic Coordinates of the Instrumentation Used in This Work

Instrument	Obs. sites	Geo. coord.	Geomag. coord.
GNSS receivers	Boa Vista	2.9°N, 60.7°W	9.6°N, 19.8°E
	Itacoatiara	3.0°S, 58.4°W	3.3°N, 19.8°E
	Colíder	10.8°S, 55.4°W	5.0°S, 19.9°E
	Cuiabá	15.6°S, 56.1°W	8.8°S, 19.7°E
All-sky imager	Boa Vista	2.5°N, 60.4°W	9.2°N, 19.8°E
DPS4	Boa Vista	2.8°N, 60.7°W	9.6°N, 19.8°E
	Campo Grande	20.5°S, 54.7°W	13.6°S, 19.7°E
FPI	São João do Cariri	7.4°S; 36.6°W	12.3°S, 21.0°E

Colíder (MTCO), and Cuiabá (CUIB). BOAV and CUIB GNSS receivers are located at geomagnetically conjugate points as well as ITAM and MTCO GNSS receivers (see Table 1). These four GNSS receivers allow us to track the EPBs from equatorial to low-latitude regions by detecting dTEC oscillations with amplitudes larger than ±1 TECU.

Figure 2 shows the dTEC plots for the GNSS receivers of Table 1 on 13 January 2015. Figure 2 (a) presents the dTEC GPS tracks for PRNs 12 and 14. In order to study the EPBs along the same magnetic meridian, only dTEC GPS tracks near the GNSS receivers were considered. In this paper, we used only dTEC GPS tracks inside a radius of 2° around each GNSS receiver. No GPS satellite track was inside the circle around ITAM GNSS receiver between 22:00 UT and 24:00 UT. Figure 2 (b), (c), and (d) present the dTEC time series for BOAV, MTCO, and CUIB GNSS receivers, respectively. As mentioned in Section 2, dTEC variations larger than ±1 TECU are considered as EPBs signatures. Figures 2b–2d show EPBs signatures near BOAV and MTCO GNSS receivers after sunset, but no signatures were observed near CUIB. Figures 2e and 2f present the BV OI630 nm unwarped image at 23:59 UT and BV ionogram at 24:00 UT, respectively. The red arrows indicate the presence of EPBs in the dTEC GPS track, BV all-sky image, and BV ionogram. Figure 2g presents Campo Grande (CG) ionogram at 24:00 UT. No spread-F could be seen in the CG ionogram. Therefore, EPBs seems to have presented an asymmetric form on 13 January 2015.

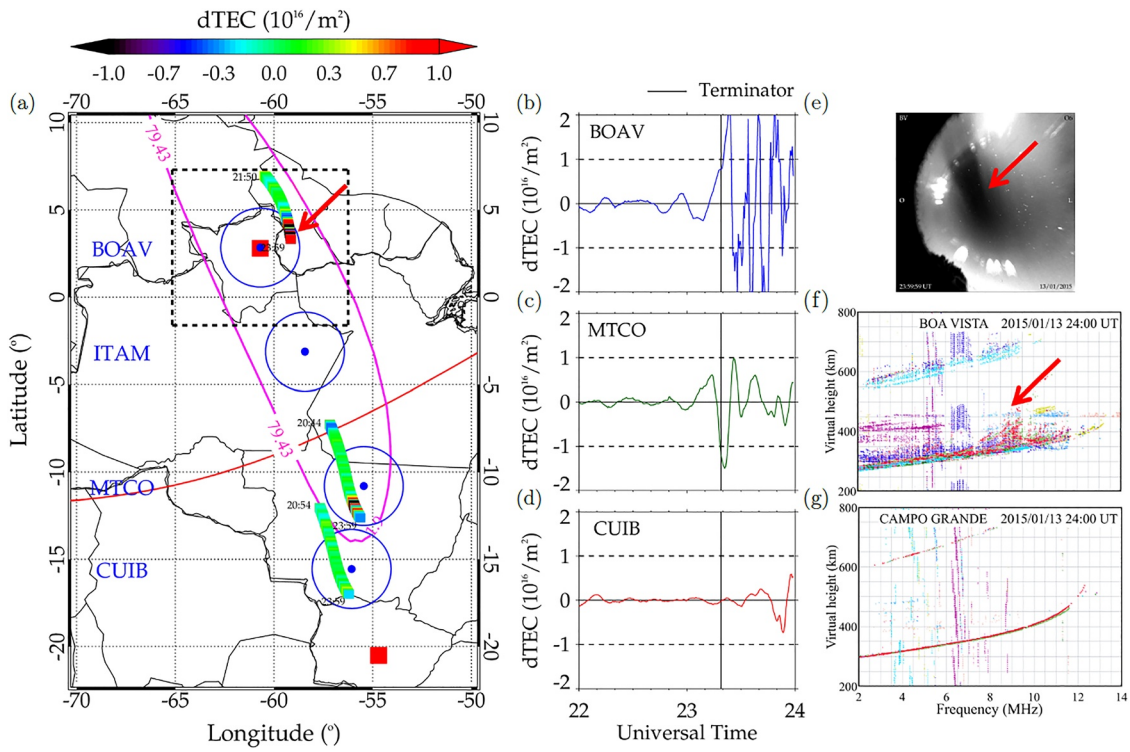

Figure 2. Detrended total electron content (dTEC) plots for the global navigation satellite systems (GNSS) receivers of Table 1 on 13 January 2015. (a) dTEC global positioning system (GPS) Tracks (PRN 14 and 22) at sub-ionospheric point. The red line, the magenta line, and the black dashed box represent the geomagnetic equator, the simulated equatorial plasma bubbles (EPB) on the height integrated OI630 nm airglow emission, and Boa Vista (BV) all-sky imager field of view, respectively. (b) Boa Vista (BOAV), (c) MTCO, and (d) Cuiabá (CUIB) dTEC time series. (e and f) present the BV OI630 nm unwarped image at 23:59 UT and BV ionogram at 24:00 UT, respectively. (g) Campo Grande (CG) ionogram at 24:00 UT. BV and CG DPS4 localization are indicated by red boxes. The red arrows indicate the EPBs occurrence in the dTEC GPS track, BV all-sky image, and BV ionogram.

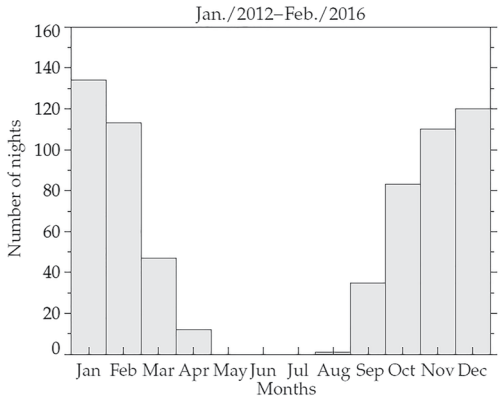

Figure 3. Equatorial plasma bubbles (EPBs) occurrence at Boa Vista (BOAV), Itacoatiara (ITAM), Colíder (MTCO), and Cuiabá (CUIB) global navigation satellite systems (GNSS) receivers between January 2012 and February 2016.

3. Results

We analyzed dTEC data obtained from BOAV, ITAM, MTCO, and CUIB GNSS receivers between January 2012 and February 2016. It was possible to analyze the EPBs meridional (north-south) development in 655 nights. This period includes both low and high solar activity with a mean solar flux (F10.7) equal to $126 \times 10^{-22} \mathrm{Wm}^{-2}\ \mathrm{Hz}^{-2}$. The EPBs occurrence observed at BOAV, ITAM, MTCO, and CUIB GNSS receivers for each month of the year is shown in Figure 3. The gray bars represent the total number of nights with EPBs. Most of EPBs were observed between October and March. The EPBs occurrence were very low between April and September. It can be noted from Figure 3, that no EPBs were observed between May and August due to the criteria of EPB identification discussed in Section 2.

3.1. EPBs Meridional Development

The analysis of the dTEC plots revealed that EPBs can present an apparent asymmetry with respect to the geomagnetic equator. We have identified two types of asymmetries. In some occasions, the north side of EPBs reached higher latitudes compared to the south side. In this case, EPBs were observed only at BOAV, ITAM, and MTCO GNSS receivers, what we called north asymmetry. In some other occasions, the south side of EPBs reached higher latitudes compared to the north side. Equatorial plasma bubbles were observed only at CUIB, MTCO, and ITAM GNSS receivers, what we called south asymmetry. Figure 4 presents the (a) north and (b) south asymmetry occurrence for the period between January 2012 and February 2016 seen in the dTEC plots. The highest north (south) asymmetry occurrence was observed from December to January (March to April and September to October) and lowest from March to April and August to September (December to January). The frequency of asymmetries is indicated over each bar. For example, in January, 15% of EPBs presented a north asymmetry, 2% presented a south asymmetry, and 83% were symmetric with respect to the geomagnetic equator. In general, EPBs presented an asymmetry in 196 nights, which correspond to ∼30% of the occurrences. It is worth to note that asymmetries are dominant during the equinox season (March, April, August, and September).

3.2. Numerical Simulation Results

The observed meridional asymmetric EPB structures represent new and relevant findings for the nighttime dynamics of the equatorial and low-latitude ionosphere. One possible cause of the asymmetry might be related to

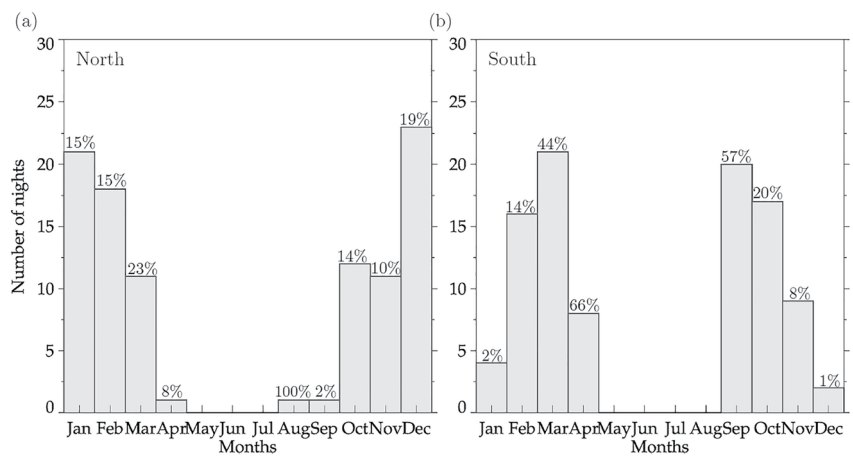

Figure 4. Monthly occurrence of equatorial plasma bubbles (EPBs) (a) north and (b) south asymmetry for the period between January 2012 and February 2016. The percentages indicate the frequency of asymmetric occurrence related to the number of nights with EPBs occurrence.

thermospheric wind system (Abdu et al., 2006; Huba & Krall, 2013; Krall et al., 2009, 2013; Maruyama, 1988; Maruyama & Matuura, 1988; Mendillo et al., 1992; Rodríguez-Zuluaga & Stolle, 2019; Zalesak & Huba, 1991).

In order to investigate the influence of the thermospheric winds on EPBs evolution, we used a numerical model based on Rayleigh-Taylor mechanism (Carrasco et al., 2014, 2017). In this simulation the ionosphere is assumed as a coordinate system, where x-, y-, and z-axis are positive eastward, southward, and upward, respectively. The main equations of the F region instability growth rate are the continuity equation for the ion O^+ (Equation 5), the divergence-free current (Equation 6) and the ions steady state velocity (Equation 7) as follows.

$$\frac{\partial N}{\partial t} = -\beta N - \vec{\nabla}\cdot\left(N\vec{V}_i\right). \tag{5}$$

$$\vec{\nabla}\cdot\vec{J} = e\vec{\nabla}\cdot\left[N\left(\vec{V}_i - \vec{V}_e\right)\right] = 0. \tag{6}$$

$$\vec{V}_{e,i} = \frac{\nu_{e,i}^2}{\nu_{e,i}^2 + \Omega_{e,i}^2}\left[\vec{U} + \frac{\Omega_{e,i}}{\nu_{e,i}}\frac{\vec{U}\times\vec{B}}{B} + \frac{\Omega_{e,i}}{\nu_{e,i}}\frac{\vec{E}}{B} + \frac{\Omega_{e,i}^2}{\nu_{e,i}^2}\frac{\vec{E}\times\vec{B}}{B^2} + \frac{\vec{g}}{\nu_{e,i}} + \frac{\Omega_{e,i}}{\nu_{e,i}^2}\frac{\vec{g}\times\vec{B}}{B}\right]. \tag{7}$$

The subscripts e and i refer to electrons and ions, respectively. The plasma is assumed to be electrically neutral, that is, $N_e = N_i = N$. β, $\vec{E}$, $\vec{B}$, $\vec{g}$, $\Omega_{e,i}$, $\vec{U}$, and $\vec{\nu}_{e,i}$ are the recombination rate for O^+, electric field, geomagnetic field, neutral wind, gravity, gyro frequency, and the collision frequency, respectively. We assumed the electric and geomagnetic fields in the following form: $\vec{E} = \vec{E}_0 - \vec{\nabla}\Phi$ and $\vec{B} = -B_0 cosI\hat{i} - B_0 senI\hat{k}$. Where $\vec{E}_0 = E_{0x}\hat{i} - E_{0z}\hat{k}$ and $\vec{\nabla} = (\partial/\partial x)\,\hat{i} + (\partial/\partial z)\,\hat{k}$. Φ, $\vec{I}$, $\vec{E}_0$, and B_0 are the electrostatic potential, geomagnetic dip angle, ambient zonal electric field, and the geomagnetic field intensity at the geomagnetic equator, respectively. $\vec{U} = \vec{U}_x\hat{i} - \vec{U}_y\hat{j}$, where $\vec{U}_x$ is the zonal wind and meridional wind. Assuming $\vec{\nu}_{e,i}/\Omega_{e,i} \ll 1$ and using Equation 6, we can obtain a equation for Φ in a differential form as follow.

$$\begin{aligned}\frac{\partial^2\Phi}{\partial x^2} + \frac{\partial^2\Phi}{\partial z^2} + \frac{\partial \ln(N)}{\partial x}\frac{\partial\Phi}{\partial x} + \frac{\partial \ln(\nu_i N)}{\partial z}\frac{\partial\Phi}{\partial z} &= \\ \left(E_{0x} + \frac{gB}{\nu_i} + \frac{\nu_i B}{\Omega_i}U\right)\frac{\partial \ln(N)}{\partial x} + \left(E_{0z} + UB - \frac{gB}{\Omega_i}\right)\frac{\partial \ln(\nu_i N)}{\partial z} + \frac{\partial(E_{0z} + UB)}{\partial z}.\end{aligned} \tag{8}$$

Moreover, Equation 5 can be written in terms of the plasma velocities components, V_{ix} and V_{iz}.

$$\frac{\partial N}{\partial t} = -\beta N - \frac{\partial}{\partial x}(NV_{ix}) - \frac{\partial}{\partial z}(NV_{iz}). \tag{9}$$

Where V_{ix} and V_{iz} are given by:

$$V_{ix} = \frac{\nu_i}{\Omega_i B}\left(E_{0x} - \frac{\partial\Phi}{\partial x}\right) - \frac{E_{0z}}{B} + \frac{1}{B}\frac{\partial\Phi}{\partial z} + \frac{g}{\Omega_i}, \tag{10}$$

$$V_{iz} = \frac{\nu_i}{\Omega_i}U - \frac{\nu_i}{\Omega_i B}\frac{\partial\Phi}{\partial z} + \frac{E_{0x}}{B} + \frac{\nu_i}{\Omega_i}\frac{E_{0z}}{B} - \frac{1}{B}\frac{\partial\Phi}{\partial x} - \frac{\nu_i}{\Omega_i^2}g. \tag{11}$$

To solve the system formed by Equations 8–11 is necessary to know how β, E_{0x}, E_{0z}, B, U, N, Ω_i, and ν_i vary in time and height. The collision frequency was obtained from Bailey and Balan (1996). E_{0x} was deduced from the BV DPS4 data using the method described by Bittencourt and Abdu (1981) and Carrasco (2005). E_{0z} was obtained from the expression provided by Forbes (1981). The geomagnetic field was obtained from IGRF12. The horizontal wind components were obtained from Horizontal Wind Model 2014 (HWM14) (Drob et al., 2015) and the neutrals densities from NRLMSISE00 (Picone et al., 2002).

Equations 8 and 9 were solved numerically using the successive over-relaxation method (SOR) (McCracken & Dorn, 1964) and predictor-corrector method with flux-corrected transport (FCT) technique (Boris & Book, 1973; Murawski & Goossens, 1994), respectively. Periodic boundary conditions were imposed in the zonal direction for both Φ and N. In the vertical direction, $\partial N/\partial z = 0$ and $\partial\Phi/\partial z = 0$ at 200 and 800 km of height. A small perturbation is applied on the bottom-side of the plasma density and described by the following.

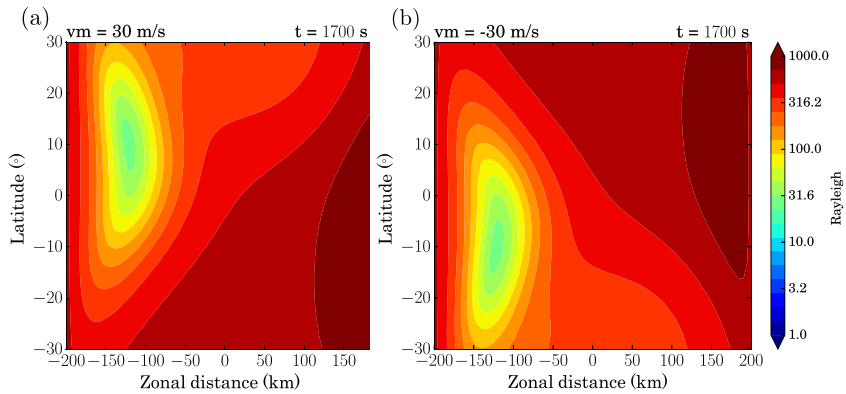

Figure 5. Contour plots of the height integrated OI630 nm airglow emission rate as a function of zonal distance and latitude using (a) $v_m = 30$ m/s and (b) $v_m = -30$ m/s.

$$N_p(x, z, 0) = N_{0p}(z)\left[1 - Acos\left(\frac{\pi x}{\lambda}\right)\right]. \quad (12)$$

Where $N(x, z, 0)$ is the plasma density at $t = 0$, N_0 is the background initial plasma density and can be obtained by International Reference Ionosphere 2016 (IRI-2016) (Bilitza et al., 2017). A is the amplitude and λ is the wavelength of the perturbation. The amplitudes of the initial perturbation were obtained following the criteria established by Carrasco and Batista (2012). More details of the simulation can be found in Carrasco et al. (2014, 2017).

Figure 5 shows contour plots of the height integrated OI630 nm airglow emission as a function of zonal distance and latitude. The geomagnetic field and atmospheric neutral densities were obtained for the geomagnetic coordinates of 0° and 19.7°E. The zonal wind (v_z) was assumed to be constant and equal to 100 m/s. In Figure 5a and 5b trans-equatorial meridional wind (v_m) was equal to 30 m/s (northward) and −30 m/s (southward), respectively. Note that a trans-equatorial meridional wind blowing to north (south) causes the north (south) asymmetry with respect to the geomagnetic equator.

Figure 6 shows a comparison between height integrated OI630 nm airglow emission as a function of zonal distance and latitude for the 56.23 Rayleighs isolines. Equatorial plasma bubbles were simulated using trans-equatorial meridional wind equal to 60 (blue), 30 (purple), −30 (green), and −60 (red) m/s. The zonal wind was constant and equal to 100 m/s. The results show that the EPBs asymmetric development and their growth rate varies with the intensity of trans-equatorial meridional wind. The increase of the meridional wind causes a greater asymmetry and a larger EPBs growth.

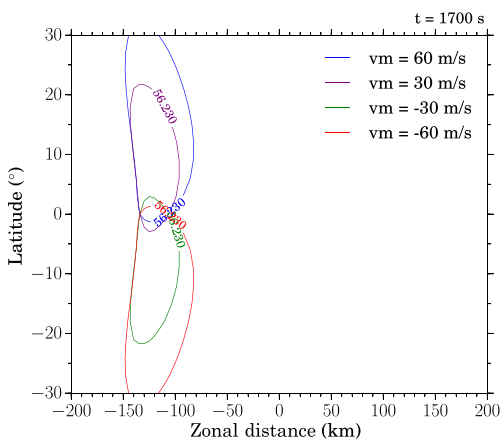

Figure 6. Comparison between height integrated OI630 nm airglow emission as a function of zonal distance and latitude for the 56.23 Rayleighs isolines using $v = 60$ (blue), 30 (purple), −30 (green), and −60 (red) m/s.

In Figure 2 it is possible to see an overlap between dTEC GPS tracks and the simulated EPB on the height integrated OI630 nm airglow emission for the night of 13 January 2015 (magenta line). In this numerical simulation, the zonal and meridional wind velocities were constant and equal to 100 and 60 m/s, respectively. The agreement with the observation and the numerical simulation indicates the importance of the meridional wind on the EPBs evolution with respect to the geomagnetic equator.

4. Discussion

The present study aims to report the EPBs meridional development (north-south) using dTEC plots, that is, to monitor the EPBs along the same magnetic meridian. Furthermore, it is to investigate a possible inter-hemispheric asymmetry and the role of a trans-equatorial meridional wind on the EPBs evolution.

It is well known that the PRE plays an important role in the EPBs development. During the daytime, an eastward electric field moves upward the

equatorial F-layer due to the $\vec{E} \times \vec{B}$ drift. At night, this electric field reverses, moving the equatorial F-layer downward (Batista et al., 1986; Rishbeth, 1981, 2000). However, before its reversal, the $\vec{E} \times \vec{B}$ drift undergoes a rapid enhancement driven by the PRE (Abdu et al., 2000). The upward drift velocity and the F-layer height create propitious conditions for EPBs evolution (Abdu, 2005; Kelley, 2009). This way, the EPBs occurrence is controlled by the PRE intensity (Abdu et al., 1981, 2001; Batista et al., 1996; Sobral et al., 2002; Tsunoda, 1985). Several studies have shown that the dependence of EPBs on the season, solar cycle, and magnetic activity can be explained as resulting from the corresponding effects on the PRE (Fejer, 1991; Fejer et al., 1991, 1999). The EPBs seasonal pattern shown in Figure 3 presented a good agreement with the PRE seasonal variation observed by different techniques (Abdu et al., 1985, 2000; Barros et al., 2018; Fejser et al., 1999; Sahai et al., 1994, 1998 , 1999, 2000).

Equatorial plasma bubbles start at the F-layer bottom-side and usually reach the topside of the ionosphere within several minutes (Carrasco et al., 2014; Huba & Krall, 2013; Krall et al., 2009; Patra et al., 2014; Sidorova & Filippov, 2014; Sultan, 1996; Zalesak & Ossakow, 1980). During the upward movement, due to the equipotential nature of the geomagnetic field lines, EPBs are mapped away from the equator to lower latitudes and altitudes (Kelley, 2009; Mendillo & Baumgardner, 1982). This EPBs upward movement stop when the field-line-integrated electron densities inside and outside the EPBs are the same or if there will be a decay of the EPBs polarization electric field (Krall et al., 2010; Mendillo et al., 2005; Narayanan et al., 2016). When EPBs stop rising they are known as fossil EPBs (Krall et al., 2010; Mendillo et al., 1992). Otsuka, Shiokawa, et al. (2002) and Sobral et al. (2009) showed highly symmetric EPBs with respect to the geomagnetic equator. Using the dTEC plots, EPBs presented a symmetric development in ∼70% of nights (Figure 4), showing a good agreement with the results presented by Otsuka, Shiokawa, et al. (2002) and Sobral et al. (2009).

However, in ∼30% of nights with EPBs occurrence they presented an apparent inter-hemispheric asymmetry. Similar asymmetry in the EPBs distribution has been reported in previous works. Su et al. (2006) studied the global distribution of the EPBs occurrence using ROCSAT satellite data during moderate to high solar activity (1999 to 2004). The authors presented a south asymmetry during both equinoxes and June solstice, and a north asymmetry during December solstice. In addition to that, Sidorova (2021) analyzed the variability of the latitudinal distributions of the EPBs occurrence probability using AE-E, ROCSAT, and ISS-b satellite data during years of increased and maximal solar activity (1978 to 1979). They showed a north asymmetry during December solstice and a south asymmetry during June solstice. Sidorova (2021) argued that these characteristics observed in the latitudinal distributions of EPB may be due to meridional (trans-equatorial) wind effects. The inter-hemispheric asymmetry shown in Figure 4 is consistent with the results presented by Su et al. (2006) and Sidorova (2021). It should be noted that Otsuka, Shiokawa, et al. (2002) analyzed only 1 case, for the night of 12 November 2001, and Sobral et al. (2009) analyzed only 6 nights between October and November 2002. With the ground-based GNSS radio-wave measurements it was possible to monitor EPBs by mapping the dTEC continuously with a high time-resolution. From a large amount of data (655 nights with EPBs occurrence), we could investigate EPBs meridional asymmetry.

The numerical simulation results presented in Figure 5 indicate that a trans-equatorial meridional wind is capable to cause an asymmetric development. In contrast to this result, most studies indicate that EPBs should be symmetric and aligned with the geomagnetic field lines, since the polarization electric field maps simultaneously to both hemispheres (Kelley, 2009; Mendillo & Baumgardner, 1982). Moreover, a uniform trans-equatorial meridional wind increases the field-line integrated Pedersen conductivity, which could decrease the EPBs growth rate (Abdu et al., 2006; Maruyama, 1988; Maruyama & Matuura, 1988; Mendillo et al., 1992; Zalesak & Huba, 1991). In other words, a northward trans-equatorial meridional winds transport plasma along the geomagnetic field lines pushing the ionosphere upward in the Southern Hemisphere and downward in the Northern Hemisphere. At lower altitudes (Northern Hemisphere), the relation between the ion-neutral collision frequency and the ion gyrofrequency $\left(\vec{\nu}_{e,i}/\Omega_{e,i}\right)$ is considerable thus the local conductivity becomes higher. On the other hand, at higher altitudes (Southern Hemisphere), $\vec{\nu}_{e,i}/\Omega_{e,i} \ll 1$ so the local conductivity becomes lower. This change in the conductivity leads to an increase in the field-line integrated Pedersen conductivity, which reduces the EPBs growth rate (Huba & Krall, 2013; Krall et al., 2009, 2013; Rodríguez-Zuluaga & Stolle, 2019). Therefore, a uniform trans-equatorial meridional wind has a stabilizing influence on EPBs, then turn them out to be fossil EPBs.

In order to see the existence of an interhemispheric asymmetry in the electron density distribution, Figure 7 shows the behavior of the F-layer virtual height at BV (blue) and CG (red) between 22:00 UT and 24:00 UT on

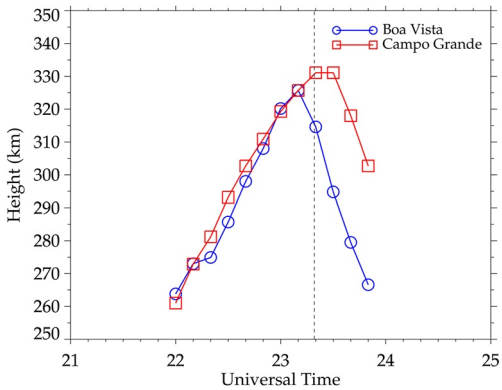

Figure 7. F-layer virtual heights at Boa Vista (blue) and Campo Grande (red) between 22:00 and 24:00 UT on the night of 13 January 2015. The vertical dashed black line represents the solar terminator at 350 km altitude.

the night of 13 January 2015, same night of the EPBs occurrence shown in Figure 2. The virtual heights were measured by a DPS4 (see Table 1 and Figure 2), which has a height resolution of 3 km (Reinisch et al., 2008) and 30° zenith angle for the oblique reflections (Laštovička et al., 2012). There is a difference of ∼40 km between the F-layer virtual height at BV and CG after 23:20 UT. There might be a trans-equatorial wind blowing to north causing this difference between the F-layer virtual heights obtained at BV and CG. Bittencourt and Sahai (1978) showed that a uniform trans-equatorial meridional wind with velocity of 200 m/s is able to produce a difference of 120 km in the F-layer heights between the geomagnetically conjugate points at 15°. For a difference of ∼40 km, it should correspond to a meridional wind with velocity of ∼66 m/s. Similar results can be seen in Krall et al. (2009), they simulated a difference of ∼40 km in the F-layer heights between the geomagnetically conjugate points using a meridional wind with velocity of ∼60 m/s, which shows a good agreement with the results presented in Figure 2.

Figure 4 showed that the EPBs asymmetries occurrence varies with the months of the year. In addition to that, EPBs are strongly influenced by the meridional wind. This way, Figure 8 presents the monthly averaged meridional wind at 350 km altitude and at 23:00 UT. The monthly averaged meridional wind was measured by a Fabry-Perot Interferometer (FPI) (blue). The FPI is located at São João do Cariri and the data were obtained between 2013 and 2014 (Figueiredo, Buriti, et al., 2017; Makela et al., 2013; Meriwether et al., 2011, 2013). Moreover, Figure 8 presents the monthly averaged meridional wind obtained by the HWM14 model for São João do Cariri (red), BV, and CG (green). The meridional winds obtained by the HWM14 model were for the period between January 2012 and February 2016, at 350 km altitude, and at 23:00 UT. The agreement of the winds between FPI and HWM14 model indicates that the HWM14 model is capable to reproduce the meridional wind behavior over the South America. Thus, Figure 8 shows that the meridional wind blows to north during the months between October and March, and blows to south between April and September. Therefore, it is possible to notice that the highest north asymmetry occurrence was observed in the months when the meridional wind was blowing to north. On the other hand, the highest south asymmetry occurrence was observed around the months when the meridional wind was blowing to south.

As mentioned before, the ratio of asymmetric to symmetric occurrence increases during the equinox season (March, April, August, and September). For example, in April the asymmetric occurrence represented 74% of EPBs occurrence. During this period of the year the meridional wind intensity is very low (see Figure 8), so there might be some additional factors causing these asymmetries. A possible cause could be due to the predominant low ionospheric electron density for this period of the year, leading to the situation where the field-line-integrated electron densities inside and outside the EPBs are the same. Another possible cause could be due to a low PRE intensity, which can reduce the EPBs growth. All these factors could contribute to an decrease in EPBs polarization electric fields, becoming then fossil and making the EPBs drift under the influence of background neutral winds, which can increase the EPBs asymmetric development occurrence during the equinox season.

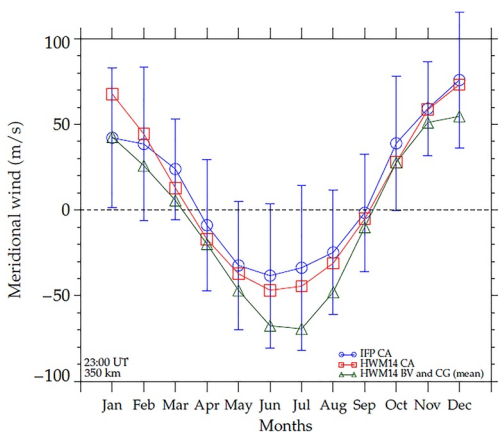

Figure 8. Monthly averaged meridional wind measured by a Fabry-Perot Interferometer at São João do Cariri (blue) and monthly averaged meridional wind obtained by HWM14 model for São João do Cariri (red), Boa Vista, and Campo Grande (green) at 350 km altitude and at 23:00 UT.

At last, as pointed out by Takahashi et al. (2016), EPBs can penetrate into the equatorial ionization anomaly (EIA) crest, making them coexist during nighttime period. Since the meridional winds can play an important role in the dynamic of the F-region ionization, the EPBs and EIA dynamics should present similar behavior. The effects of the meridional winds on the EIA dynamics have been investigated by several authos (Appleton, 1946; Balan et al., 2018; Balan & Bailey, 1996; Batista et al., 2011; Croom et al., 1959; Dang et al., 2016, 2017; Duncan, 1960; Huang et al., 2018; Kepkar et al., 2019; Krall et al., 2009). Lin et al. (2007) studied the structure and motion of the EIA using worldwide 3-D ionospheric images provided by FORMOSAT-3/

COSMIC for the period from July to August of 2006. The authors showed that the ionization is transported from summer to winter hemisphere by meridional wind. Venkatesh et al. (2014) used 8 ground-based GNSS receivers to calculate the day-to-day variability of the TEC from 2010 to 2013 over the Brazilian longitude of 45°. The results clearly showed that during December, January, and February the Southern EIA crest was more close to the geomagnetic equator and presented a reduction in its TEC value when compared to March, April, September, and October. Using similar methodology, Dias et al. (2020) used 35 ground-based GNSS receivers to study the EIA over three different Brazilian longitudinal sectors during 2016. The results clearly showed an seasonal inter-hemispheric asymmetries in the EIA electron distribution, where the EIA is pushed northward during January, November, and December and pushed southward during March, April, September, and October. Therefore, the EPBs asymmetric development seasonal variation (Figure 4) and monthly averaged meridional wind (Figure 8) shows also a good agreement with the EIA inter-hemispheric asymmetry behavior presented in the literature.

5. Conclusion

We reported the EPBs characteristics observed by dTEC plots obtained from data taken at BOAV, ITAM, MTCO, and CUIB GNSS receivers between January 2012 and February 2016. In addition to that, a numerical simulation was used to study the causes of the EPBs asymmetric development with respect to the geomagnetic equator. Our main conclusions are as follows:

1. From the 655 EPBs observed, in 459 cases (∼70%) the EPBs presented a symmetric development with respect to the geomagnetic equator. In 196 cases (∼30%) the EPBs presented an inter-hemispheric asymmmetry. The EPBs presented two types of asymmetry. A north asymmetry, when the EPBs presented a displacement to north of the geomagnetic equator, or a south asymmetry, when the EPBs presented displacement to south. The highest north (south) asymmetry occurrence was observed from December to January (March to April and September to October), and lowest from March to April and August to September (December to January).
2. Numerical simulations results of the EPBs evolution suggested that these asymmetries are due to a trans-equatorial meridional wind. A trans-equatorial meridional wind blowing to north (south) causes a displacement of EPBs to north (south) of the geomagnetic equator. A northward (southward) trans-equatorial meridional winds transport plasma along the geomagnetic field lines pushing the ionosphere upward in the Southern (Northern) Hemisphere and downward in the Northern (Southern) Hemisphere, increasing the field-line integrated Pedersen conductivity, which could decrease the EPBs growth rate.

Data Availability Statement

The GPS, all-sky, and DPS4 data used in this work were provided via FTP servers of RBMC (2021) and Embrace (2021). FPI data were provided by Madrigal (2021).

Acknowledgments
This work was supported by Conselho Nacional de Desenvolvimento Científico e Tecnológico (CNPq) under contract 301988/2021-8. H. Takahashi thanks CNPq (Grant 310927/2020-0). C.M. Wrasse thanks CNPq (Grant 314972/2020-0). C.A.O.B. Figueiredo thanks Fundação de Amparo à Pesquisa do Estado de São Paulo (FAPESP) (grants 2018/09066-8 and 2019/22548-4).

References

Abdu, M. (2001). Outstanding problems in the equatorial ionosphere–thermosphere electrodynamics relevant to spread f. *Journal of Atmospheric and Solar-Terrestrial Physics*, *63*(9), 869–884. https://doi.org/10.1016/s1364-6826(00)00201-7

Abdu, M. (2005). Equatorial ionosphere–thermosphere system: Electrodynamics and irregularities. *Advances in Space Research*, *35*(5), 771–787. https://doi.org/10.1016/j.asr.2005.03.150

Abdu, M., Batista, I., Reinisch, B., De Souza, J., Sobral, J., Pedersen, T., et al. (2009). Conjugate point equatorial experiment (copex) campaign in Brazil: Electrodynamics highlights on spread f development conditions and day-to-day variability. *Journal of Geophysical Research*, *114*(A4). https://doi.org/10.1029/2008ja013749

Abdu, M., Batista, I., Reinisch, B., MacDougall, J., Kherani, E., & Sobral, J. (2012). Equatorial range spread f echoes from coherent backscatter, and irregularity growth processes, from conjugate point digital ionograms. *Radio Science*, *47*(6). https://doi.org/10.1029/2012rs005002

Abdu, M., Batista, I., Takahashi, H., MacDougall, J., Sobral, J., Medeiros, A., & Trivedi, N. (2003). Magnetospheric disturbance induced equatorial plasma bubble development and dynamics: A case study in Brazilian sector. *Journal of Geophysical Research*, *108*(A12), 1449. https://doi.org/10.1029/2002ja009721

Abdu, M., Bittencourt, J., & Batista, I. (1981). Magnetic declination control of the equatorial f region dynamo electric field development and spread f. *Journal of Geophysical Research*, *86*(A13), 11443–11446. https://doi.org/10.1029/ja086ia13p11443

Abdu, M., Iyer, K. N., de Medeiros, R., Batista, I. S., & Sobral, J. H. (2006). Thermospheric meridional wind control of equatorial spread f and evening prereversal electric field. *Geophysical Research Letters*, *33*(7), L07106. https://doi.org/10.1029/2005gl024835

Abdu, M., Medeiros, R., Sobral, J., & Bittencourt, J. (1983). Spread f plasma bubble vertical rise velocities determined from spaced ionosonde observations. *Journal of Geophysical Research*, *88*(A11), 9197–9204. https://doi.org/10.1029/ja088ia11p09197

Abdu, M., Muralikrishna, P., Batista, I., & Sobral, J. (1991). Rocket observation of equatorial plasma bubbles over natal, Brazil, using a high-frequency capacitance probe. *Journal of Geophysical Research*, *96*(A5), 7689–7695. https://doi.org/10.1029/90ja02384

Abdu, M., Sobral, J., Nelson, O., & Batista, I. (1985). Solar cycle related range type spread-f occurrence characteristics over equatorial and low latitude stations in Brazil. *Journal of Atmospheric and Terrestrial Physics*, *47*(10), 901–905. https://doi.org/10.1016/0021-9169(85)90065-0

Abdu, M. A. (2016). Electrodynamics of ionospheric weather over low latitudes. *Geoscience Letters*, *3*(1), 11. https://doi.org/10.1186/s40562-016-0043-6

Abdu, M. A., Kherani, E. A., Batista, I. S., Paula, E. R., Fritts, D. C., & Sobral, J. H. A. (2009). Gravity wave initiation of equatorial spread f/plasma bubble irregularities based on observational data from the spreadfex campaign. *Annales Geophysicae*, *27*(7), 2607–2622. https://doi.org/10.5194/angeo-27-2607-2009

Abdu, M. A., Sobral, J. H. A., & Batista, I. S. (2000). Equatorial spread f statistics in the American longitudes: Some problems relevant to ESF description in the IRI scheme. *Advances in Space Research*, *25*(1), 113–124. https://doi.org/10.1016/s0273-1177(99)00907-2

Agyei-Yeboah, E., Fagundes, P. R., Tardelli, A., Pillat, V. G., Pignalberi, A., Kavutarapu, V., et al. (2021). Ground and satellite-based observations of ionospheric plasma bubbles and blobs at 5.65°latitude in the Brazilian sector. *Advances in Space Research*, *67*(8), 2416–2438. https://doi.org/10.1016/j.asr.2021.01.034

Appleton, E. V. (1946). Two anomalies in the ionosphere. *Nature*, *157*(3995), 691. https://doi.org/10.1038/157691a0

Arruda, D. C., Sobral, J., Abdu, M., Castilho, V. M., Takahashi, H., Medeiros, A., & Buriti, R. (2006). Theoretical and experimental zonal drift velocities of the ionospheric plasma bubbles over the Brazilian region. *Advances in Space Research*, *38*(11), 2610–2614. https://doi.org/10.1016/j.asr.2006.05.015

Bailey, G. J., & Balan, N. (1996). *A low-latitude ionosphere-plasmasphere model*. Schunk.

Balan, N., & Bailey, G. (1996). Modeling studies of equatorial plasma fountain and equatorial anomaly. *Advances in Space Research*, *18*(3), 107–116. https://doi.org/10.1016/0273-1177(95)00848-9

Balan, N., Liu, L., & Le, H. (2018). A brief review of equatorial ionization anomaly and ionospheric irregularities. *Earth and Planetary Physics*, *2*(4), 257–275. https://doi.org/10.26464/epp2018025

Barros, D., Takahashi, H., Wrasse, C. M., & Figueiredo, C. A. O. (2018). Characteristics of equatorial plasma bubbles observed by TEC map based on ground-based GNSS receivers over South America. *Annales Geophysicae*, *36*, 91–100. https://doi.org/10.5194/angeo-36-91-2018

Basu, S., Groves, K., Quinn, J., & Doherty, P. (1999). A comparison of TEC fluctuations and scintillations at ascension island. *Journal of Atmospheric and Solar-Terrestrial Physics*, *61*(16), 1219–1226. https://doi.org/10.1016/s1364-6826(99)00052-8

Batista, I., Abdu, M., & Bittencourt, J. (1986). Equatorial F region vertical plasma drifts: Seasonal and longitudinal asymmetries in the American sector. *Journal of Geophysical Research*, *91*(A11), 12064. https://doi.org/10.1029/ja091ia11p12055

Batista, I., Medeiros, R. d., Abdu, M., Souza, J. d., Bailey, G., & Paula, E. d. (1996). Equatorial ionospheric vertical plasma drift model over the Brazilian region. *Journal of Geophysical Research*, *101*(A5), 10887–10892. https://doi.org/10.1029/95ja03833

Batista, I. S., Diogo, E. M., Souza, J. R., Abdu, M. A., & Bailey, G. J. (2011). Equatorial ionization anomaly: The role of thermospheric winds and the effects of the geomagnetic field secular variation. In *Aeronomy of the Earth's Atmosphere and Ionosphere* (pp. 317–328). Springer.

Bilitza, D., Altadill, D., Truhlik, V., Shubin, V., Galkin, I., Reinisch, B., & Huang, X. (2017). International reference ionosphere 2016: From ionospheric climate to real-time weather predictions. *Space Weather*, *15*(2), 418–429. https://doi.org/10.1002/2016sw001593

Bittencourt, J., & Abdu, M. (1981). A theoretical comparison between apparent and real vertical ionization drift velocities in the equatorial F region. *Journal of Geophysical Research*, *86*(A4), 2451–2454. https://doi.org/10.1029/ja086ia04p02451

Bittencourt, J., & Sahai, Y. (1978). F-region neutral winds from ionosonde measurements of HMF2 at low latitude magnetic conjugate regions. *Journal of Atmospheric and Terrestrial Physics*, *40*(6), 669–676. https://doi.org/10.1016/0021-9169(78)90124-1

Boris, J. P., & Book, D. L. (1973). Flux-corrected transport. I. Shata, a fluid transport algorithm that works. *Journal in Computation in Physics*, *11*(1), 38–69. https://doi.org/10.1016/0021-9991(73)90147-2

Carrasco, A., & Batista, I. (2012). Estimation of the initial amplitude of plasma bubble seed perturbation from ionograms. *Radio Science*, *47*(2). https://doi.org/10.1029/2011rs004862

Carrasco, A., Batista, I., & Abdu, M. (2014). Numerical simulation of equatorial plasma bubbles over Cachimbo: Copex campaign. *Advances in Space Research*, *54*(3), 443–455. https://doi.org/10.1016/j.asr.2013.10.017

Carrasco, A., Batista, I., Sobral, J., & Abdu, M. (2017). Spread F modeling over Brazil. *Journal of Atmospheric and Solar-Terrestrial Physics*, *161*, 98–104. https://doi.org/10.1016/j.jastp.2017.06.015

Carrasco, A. J. (2005). *O pico pré-inversão na deriva vertical de plasma e a camada e esporádica*.

Coco, D. S., Coker, C., Dahle, S. R., & Clynch, J. R. (1991). Variability of GPS satellite differential group delay biases. *IEEE Transactions on Aerospace and Electronic Systems*, *27*(6), 931–938. https://doi.org/10.1109/7.104264

Croom, S., Robbins, A., & Thomas, J. (1959). Two anomalies in the behaviour of the f 2 layer of the ionosphere. *Nature*, *184*(4704), 2003–2004. https://doi.org/10.1038/1842003a0

Dang, T., Luan, X., Lei, J., Dou, X., & Wan, W. (2016). A numerical study of the interhemispheric asymmetry of the equatorial ionization anomaly in solstice at solar minimum. *Journal of Geophysical Research: Space Physics*, *121*(9), 9099–9110. https://doi.org/10.1002/2016ja023012

Dang, T., Wang, W., Burns, A., Dou, X., Wan, W., & Lei, J. (2017). Simulations of the ionospheric annual asymmetry: Sun-earth distance effect. *Journal of Geophysical Research: Space Physics*, *122*(6), 6727–6736. https://doi.org/10.1002/2017ja024188

Dear, R. M., & Mitchell, C. N. (2006). GPS interfrequency biases and total electron content errors in ionospheric imaging over Europe. *Radio Science*, *41*(6). https://doi.org/10.1029/2005rs003269

de Jesus, R., Batista, I., Takahashi, H., de Paula, E., Barros, D., Figueiredo, C., et al. (2020). Morphological features of ionospheric scintillations during high solar activity using GPS observations over the South American sector. *Journal of Geophysical Research: Space Physics*, *125*(3), 2019JA027441. https://doi.org/10.1029/2019ja027441

De Rezende, L., De Paula, E., Kantor, I., & Kintner, P. (2007). Mapping and survey of plasma bubbles over Brazilian territory. *Journal of Navigation*, *60*(01), 69–81. https://doi.org/10.1017/s0373463307004006

Dias, M., Fagundes, P., Venkatesh, K., Pillat, V., Ribeiro, B., Seemala, G., & Arcanjo, M. (2020). Daily and monthly variations of the equatorial ionization anomaly (EIA) over the Brazilian sector during the descending phase of the solar cycle 24. *Journal of Geophysical Research: Space Physics*, *125*(9), e2020JA027906. https://doi.org/10.1029/2020ja027906

Doherty, P., Raffi, E., Klobuchar, J., & El-Arini, M. B. (1994). Statistics of time rate of change of ionospheric range delay. *Proceedings of ION GPS-94* (Vol. 2). Citeseer.

Drob, D. P., Emmert, J. T., Meriwether, J. W., Makela, J. J., Doornbos, E., Conde, M., et al. (2015). An update to the horizontal wind model (HWM): The quiet time thermosphere. *Earth and Space Science*, *2*(7), 301–319. https://doi.org/10.1002/2014ea000089

Duncan, R. (1960). The equatorial f-region of the ionosphere. *Journal of Atmospheric and Terrestrial Physics*, *18*(2–3), 89–100. https://doi.org/10.1016/0021-9169(60)90081-7

Embrace (2021). Estudo e monitoramento brasileiro do clima espacial website. available at http://www2.inpe.br/climaespacial/portal/en/

Fagundes, P., Sahai, B. J., Bittencourt, J. Y., & Takahashi, H. (1995). Relationship between generation of equatorial f-region plasma bubbles and thermospheric dynamics. *Advances in Space Research*, *16*(5), 117–120. https://doi.org/10.1016/0273-1177(95)00180-m

Fejer, B. G. (1991). Low latitude electrodynamic plasma drifts: A review. *Journal of Atmospheric and Solar-Terrestrial Physics*, *53*(8), 677–693. https://doi.org/10.1016/0021-9169(91)90121-m

Fejer, B. G., Paula, E. d., Gonzalez, S., & Woodman, R. (1991). Average vertical and zonal F region plasma drifts over Jicamarca. *Journal of Geophysical Research*, *96*(A8), 13901–13906. https://doi.org/10.1029/91ja01171

Fejer, B. G., Scherliess, L., & De Paula, E. (1999). Effects of the vertical plasma drift velocity on the generation and evolution of equatorial spread f. *Journal of Geophysical Research*, *104*(A9), 19859. https://doi.org/10.1029/1999ja900271

Figueiredo, C., Takahashi, H., Wrasse, C., Otsuka, Y., Shiokawa, K., & Barros, D. (2018). Medium-scale traveling ionospheric disturbances observed by detrended total electron content maps over Brazil. *Journal of Geophysical Research: Space Physics*, *123*(3), 2215–2227. https://doi.org/10.1002/2017ja025021

Figueiredo, C., Wrasse, C., Takahashi, H., Otsuka, Y., Shiokawa, K., & Barros, D. (2017). Large-scale traveling ionospheric disturbances observed by GPS DTEC maps over north and South America on saint Patrick's day storm in 2015. *Journal of Geophysical Research: Space Physics*, *122*(4), 4755–4763. https://doi.org/10.1002/2016ja023417

Figueiredo, C. A. O., Buriti, R. A., Paulino, I., Meriwether, J. W., Makela, J. J., Batista, I. S., et al. (2017). Effects of the midnight temperature maximum observed in the thermosphere–ionosphere over the northeast of Brazil. *Annales Geophysicae*, *35*(4), 953–963. https://doi.org/10.5194/angeo-35-953-2017

Forbes, M. J. (1981). The equatorial electrojet. *Reviews of Geophysics*, *19*(3), 469–504. https://doi.org/10.1029/rg019i003p00469

Haase, J. S., Dautermann, T., Taylor, M. J., Chapagain, N., Calais, E., & Pautet, D. (2011). Propagation of plasma bubbles observed in Brazil from GPS and airglow data. *Advances in Space Research*, *47*(10), 1758–1776. https://doi.org/10.1016/j.asr.2010.09.025

Haerendel, G. (1973). *Theory of equatorial spread-f*. Report Max-Planck Institute.

Huang, C., Burke, W., Machuzak, J., Gentile, L., & Sultan, P. (2002). Equatorial plasma bubbles observed by DMSP satellites during a full solar cycle: Toward a global climatology. *Journal of Geophysical Research*, *107*(A12), SIA7-1–SIA7-10. https://doi.org/10.1029/2002ja009452

Huang, C., de La Beaujardière, O., Roddy, P., Hunton, D., Ballenthin, J. H. M. R., & Pfaff, R. (2013). Large-scale quasiperiodic plasma bubbles: C/NOFS observations and causal mechanism. *Journal of Geophysical Research*, *118*(6), 3602–3612. https://doi.org/10.1002/jgra.50338

Huang, H., Lu, X., Liu, L., Wang, W., & Li, Q. (2018). Transition of interhemispheric asymmetry of equatorial ionization anomaly during solstices. *Journal of Geophysical Research: Space Physics*, *123*(12), 10–283. https://doi.org/10.1029/2018ja026055

Huba, J., & Krall, J. (2013). Impact of meridional winds on equatorial spread F: Revisited. *Geophysical Research Letters*, *40*(7), 1268–1272. https://doi.org/10.1002/grl.50292

Hysell, D., Kelley, M., Swartz, W., & Woodman, R. (1990). Seeding and layering of equatorial spread F by gravity waves. *Journal of Geophysical Research*, *95*(A10), 17253–17260. https://doi.org/10.1029/ja095ia10p17253

Kelley, M. C. (2009). *The Earth's ionosphere*. Elsevier.

Kepkar, A., Arras, C., Wickert, J., Schuh, H., Alizadeh, M., & Tsai, L.-C. (2019). Global climatology of equatorial plasma bubbles based on GPS radio occultation from formosat-3/cosmic. *Annales Geophysicae Discussions*.

Krall, J., Huba, J., Joyce, G., & Zalesak, S. (2009). Three-dimensional simulation of equatorial spread-f with meridional wind effects. *Annales Geophysicae*, *27*(5), 1821–1830. https://doi.org/10.5194/angeo-27-1821-2009

Krall, J., Huba, J., Ossakow, S., & Joyce, G. (2010). Why do equatorial ionospheric bubbles stop rising? *Geophysical Research Letters*, *37*(9). https://doi.org/10.1029/2010gl043128

Krall, J., Huba, J. D., Joyce, M., Hei, M., & Hei, G. (2013). Simulation of the seeding of equatorial spread F by circular gravitywaves. *Geophysical Research Letters*, *40*, 1–5. https://doi.org/10.1029/2012gl054022

Laštovička, J., Boška, J., Burešová, D., & Kouba, D. (2012). High historical values of foes—Reality or artefact? *Journal of Atmospheric and Solar-Terrestrial Physics*, *74*, 51–54. https://doi.org/10.1016/j.jastp.2011.10.008

Li, Q., Zhu, Y., Fang, K., & Fang, J. (2020). Statistical study of the seasonal variations in TEC depletion and the roti during 2013–2019 over Hong Kong. *Sensors*, *20*(21), 6200. https://doi.org/10.3390/s20216200

Lin, C., Liu, J., Fang, T., Chang, P., Tsai, H., Chen, C., & Hsiao, C. (2007). Motions of the equatorial ionization anomaly crests imaged by Formosat-3/cosmic. *Geophysical Research Letters*, *34*(19), L19101. https://doi.org/10.1029/2007gl030741

Madrigal (2021). Cedar madrigal database website. Retrieved from http://cedar.openmadrigal.org

Magdaleno, S., Herraiz, M., Altadill, D., & Benito, A. (2017). Climatology characterization of equatorial plasma bubbles using GPS data. *Journal of Space Weather and Space Climate*, *7*, A3. https://doi.org/10.1051/swsc/2016039

Makela, J., Ledvina, B., Kelley, M., & Kintner, P. (2004). Analysis of the Seasonal Variations of Equatorial Plasma Bubble Occurrence Observed from Haleakala, Hawaii. *Annales Geophysicae*, *22*, 3109–3121.

Makela, J. J., Fisher, D. J., Meriwether, J. W., Buriti, R. A., & Medeiros, A. F. (2013). Near-continual ground-based nighttime observations of thermospheric neutral winds and temperatures over equatorial Brazil from 2009 to 2012. *Journal of Atmospheric and Solar-Terrestrial Physics*, *103*, 94–102. https://doi.org/10.1016/j.jastp.2012.11.019

Mannucci, A. J., Wilson, B. D., Yuan, D. N., Ho, C. H., Lindqwister, U. J., & Runge, T. F. (1998). A global mapping technique for GPS-derived ionospheric total electron content measurements. *Radio Science*, *33*(3), 565–582. https://doi.org/10.1029/97rs02707

Maruyama, T. (1984). Modeling study of equatorial ionospheric height and spread-F ocurrence. *Journal of Geophysical Research*, *101*(A3), 5157–5163.

Maruyama, T. (1988). A diagnostic model for equatorial spread F, 1, model description and application to electric field and neutral wind effects. *Journal of Geophysical Research*, *93*(A12), 14611–14622. https://doi.org/10.1029/ja093ia12p14611

Maruyama, T., & Matuura, N. (1988). A diagnostic model for equatorial spread F, 1, model description and application to electric field and neutral wind effects. *Journal of Geophysical Research*, *93*(A12), 14611. https://doi.org/10.1029/ja093ia12p14611

McCracken, D. D., & Dorn, W. S. (1964). *Numerical methods and FORTRAN programming*. Wiley.

McNamara, L., Caton, R., Parris, R., Pedersen, T., Thompson, D., Wiens, K., & Groves, K. (2013). Signatures of equatorial plasma bubbles in VHF satellite scintillations and equatorial ionograms. *Radio Science*, *48*(2), 89–101. https://doi.org/10.1002/rds.20025

Mendillo, M., & Baumgardner, J. (1982). Airglow characteristics of equatorial plasma depletions. *Journal of Geophysical Research*, *87*(A9), 7641–7647. https://doi.org/10.1029/ja087ia09p07641

Mendillo, M., Sultan, P. J., Pi, X., & Tsunoda, R. (1992). Onset conditions for equatorial spread F. *Journal of Geophysical Research*, *97*(13), 865. https://doi.org/10.1029/92ja00647

Mendillo, M., Zesta, E., Shodhan, S., Sultan, P. J., Doe, R., Sahai, Y., & Baumgardner, J. (2005). Observations and modeling of the coupled latitude-altitude patterns of equatorial plasma depletions. *Journal of Geophysical Research*, *110*(A9). https://doi.org/10.1029/2005ja011157

Meriwether, J., Makela, J., Fisher, D., Buriti, R., Medeiros, A., Akmaev, R., et al. (2013). Comparisons of thermospheric wind and temperature measurements in equatorial Brazil to whole atmosphere model predictions. *Journal of Atmospheric and Solar-Terrestrial Physics*, *103*, 103–112. https://doi.org/10.1016/j.jastp.2013.04.002

Meriwether, J., Makela, J., Huang, Y., Fisher, D., Buriti, R., Medeiros, A., & Takahashi, H. (2011). Climatology of the night time equatorial thermospheric winds and temperatures over Brazil near solar minimum. *Journal of Geophysical Research*, *116*(A4). https://doi.org/10.1029/2011ja016477

Muralikrishna, P., Vieira, L. P., & Abdu, M. A. (2007). Spectral features of e-and f-region plasma irregularities as observed by rocket-borne electron density probes from Brazil. *Revista Brasileira de Geofisica*, *25*, 115–128. https://doi.org/10.1590/s0102-261x2007000600014

Murawski, K., & Goossens, M. (1994). Flux corrected transport method for MHD plasma: Description of the numerical algorithm and tests. *Astronomy and Astrophysics*, *286*, 943–951.

Narayanan, V., Gurubaran, S., Shiokawa, K., & Emperumal, K. (2016). Shrinking equatorial plasma bubbles. *Journal of Geophysical Research: Space Physics*, *121*(7), 6924–6935. https://doi.org/10.1002/2016ja022633

Otsuka, Y., Ogawa, T., Saito, A., Tsugawa, T., Fukao, S., & Miyazaki, S. A. (2002). New technique for mapping of total electron content using GPS network in Japan. *Earth Planets and Space*, *54*(1), 63–70. https://doi.org/10.1186/bf03352422

Otsuka, Y., Shiokawa, K., Ogawa, T., & Wilkinson, P. (2002). Geomagnetic conjugate observations of equatorial airglow depletions. *Geophysical Research Letters*, *29*(15), 43-1–43-4. https://doi.org/10.1029/2002gl015347

Park, J., Lühr, H., & Noja, M. (2015). Three-dimensional morphology of equatorial plasma bubbles deduced from measurements onboard champ. *Annals of Geophysics*, *33*(1), 129–135. https://doi.org/10.5194/angeo-33-129-2015

Patra, A., Srinivasulu, P., Chaitanya, P. P., Rao, M. D., & Jayaraman, A. (2014). First results on low-latitude E and F region irregularities obtained using the gadanki ionospheric radar interferometer. *Journal of Geophysical Research: Space Physics*, *119*(12), 10–276. https://doi.org/10.1002/2014ja020604

Paulino, I., Medeiros, A. F., Buriti, R. A., Takahashi, H., Sobra, J. H. A., & Gobbi, D. (2011). Plasma bubble zonal drift characteristics observed by airglow images over Brazilian tropical region. *Advances in Space Research*, *29*(2), 239–246. https://doi.org/10.1590/s0102-261x2011000200003

Picone, J., Hedin, A., Drob, D. P., & Aikin, A. (2002). Nrlmsise-00 empirical model of the atmosphere: Statistical comparisons and scientific issues. *Journal of Geophysical Research*, *107*(A12), SIA15-16. SIA–15. https://doi.org/10.1029/2002ja009430

Pimenta, A., Bittencourt, J., Fagundes, P., Sahai, Y., Buriti, R., Takahashi, H., & Taylor, M. J. (2003). Ionospheric plasma bubble zonal drifts over the tropical region: A study using oi 630nm emission all-sky images. *Journal of Atmospheric and Solar-Terrestrial Physics*, *65*(10), 1117–1126. https://doi.org/10.1016/s1364-6826(03)00149-4

RBMC. (2021). Rede brasileira de monitoramento continuo dos sistemas gnss website. Retrieved from https://www.ibge.gov.br/en/geosciences/geodetic-positioning/geodetic-networks/

Reinisch, B. W., Galkin, I. A., Khmyrov, G. M., Kozlov, A. V., Lisysyan, I. A., Bibl, K., et al. (2008). *Advancing digisonde technology: The DPS-4d AIP Conference Proceedings*. (Vol. 974, pp. 127–143). American Institute of Physics.

Rishbeth, H. (1981). The F-region dynamo. *Journal of Atmospheric and Terrestrial Physics*, *43*(5–6), 387–392. https://doi.org/10.1016/0021-9169(81)90102-1

Rishbeth, H. (2000). The equatorial f-layer: Progress and puzzles. *Annales Geophysicae*, *18*, 730–739.

Rodríguez-Zuluaga, J., & Stolle, C. (2019). Interhemispheric field-aligned currents at the edges of equatorial plasma depletions. *Scientific Reports*, *9*(1), 1–8. https://doi.org/10.1038/s41598-018-37955-z

Sahai, Y., Aarons, J., Mendillo, M., Baumgardner, J., Bittencourt, J., & Takahashi, H. (1994). Oi 630 nm imaging observations of equatorial plasma depletions at 16°S dip latitude. *Journal of Atmospheric and Terrestrial Physics*, *56*(11), 1461–1475. https://doi.org/10.1016/0021-9169(94)90113-9

Sahai, Y., Fagundes, P., & Bittencourt, J. (2000). Transequatorial F-region ionospheric plasma bubbles: Solar cycle effects. *Journal of Atmospheric and Solar-Terrestrial Physics*, *62*(15), 1377–1383. https://doi.org/10.1016/s1364-6826(00)00179-6

Sahai, Y., Fagundes, P., Bittencourt, J., & Abdu, M. (1998). Occurrence of large scale equatorial f-region plasma depletions during geo-magnetic disturbances. *Journal of Atmospheric and Solar-Terrestrial Physics*, *60*(16), 1593–1604. https://doi.org/10.1016/s1364-6826(98)00097-2

Sahai, Y., Fagundes, P. R., & Bittencourt, J. A. (1999). Solar cycle effects on large scale equatorial F-region plasma depletions. *Advances in Space Research*, *24*(11), 1477–1480. https://doi.org/10.1016/s0273-1177(99)00709-7

Sardon, E., & Zarraoa, N. (1997). Estimation of total electron content using GPS data: How stable are the differential satellite and receiver instrumental biases. *Radio Science*, *32*(5), 1899–1910. https://doi.org/10.1029/97rs01457

Sau, S., Narayanan, V., Gurubaran, S., Ghodpage, R. N., & Patil, P. (2017). First observation of interhemispheric asymmetry in the EPBS during the st. Patrick's day geomagnetic storm of 2015. *Journal of Geophysical Research: Space Physics*, *122*(6), 6679–6688. https://doi.org/10.1002/2017ja024213

Shiokawa, K., Otsuka, Y., Ogawa, T., & Wilkinson, P. (2004). Time evolution of high-altitude plasma bubbles imaged at geomagnetic conjugate points. *Annales Geophysicae*, *22*(9), 3137–3143. https://doi.org/10.5194/angeo-22-3137-2004

Sidorova, L. (2021). Equatorial plasma bubbles: Variability of the latitudinal distribution with altitude. *Geomagnetism and Aeronomy*, *61*(4), 508–519. https://doi.org/10.1134/s0016793221040162

Sidorova, L., & Filippov, S. (2014). Plasma bubbles in the topside ionosphere: Estimations of the survival possibility. *Journal of Atmospheric and Solar-Terrestrial Physics*, *119*, 35–41. https://doi.org/10.1016/j.jastp.2014.06.013

Sobral, J., Abdu, M., Pedersen, T., Castilho, V. M., Arruda, D., Muella, M., et al. (2009). Ionospheric zonal velocities at conjugate points over Brazil during the copex campaign: Experimental observations and theoretical validations. *Journal of Geophysical Research*, *114*(A4). https://doi.org/10.1029/2008ja013896

Sobral, J., Abdu, M., Takahashi, H., Taylor, M. J., De Paula, E., Zamlutti, C., et al. (2002). Ionospheric plasma bubble climatology over Brazil based on 22 years (1977–1998) of 630nm airglow observations. *Journal of Atmospheric and Solar-Terrestrial Physics*, *64*(12), 1517–1524. https://doi.org/10.1016/s1364-6826(02)00089-5

Sobral, J. H. A., Abdu, M. A., Batistai, I. S., Zamlutti, C. J., & Borba, G. L. (1981). Wave disturbances in the low latitude ionosphere and equatorial ionospheric plasma depletions. *Journal of Geophysical Research*, *86*(A3), 1374–1378. https://doi.org/10.1029/ja086ia03p01374

Su, S.-Y., Liu, C., Ho, H., & Chao, C. (2006). Distribution characteristics of topside ionospheric density irregularities: Equatorial versus midlatitude regions. *Journal of Geophysical Research*, *111*(A6), A06305. https://doi.org/10.1029/2005ja011330

Sultan, P. J. (1996). Linear theory and modeling of the Rayleigh-Taylor instability leading to the ocurrence of equatorial spread-F. *Journal of Geophysical Research*, *101*(A12), 26875–26891. https://doi.org/10.1029/96ja00682

Takahashi, H., Costa, S., Otsuka, Y., Shiokawa, K., Monico, J. F. G., Paula, E., et al. (2014). Diagnostics of equatorial and low latitude ionosphere by tec mapping over Brazil. *Advances in Space Research*, *54*(3), 385–394. https://doi.org/10.1016/j.asr.2014.01.032

Takahashi, H., Essien, P., Figueiredo, C., Wrasse, C., Barros, D., Abdu, M., et al. (2021). Multi-instrument study of longitudinal wave structures for plasma bubble seeding in the equatorial ionosphere. *Earth and Planetary Physics*, *5*(5), 368–377. https://doi.org/10.26464/epp2021047

Takahashi, H., Wrasse, C., Denardini, C., Pádua, M., Paula, E., Costa, S., et al. (2016). Ionospheric tec weather map over South America. *Space Weather*, *14*(11), 937–949. https://doi.org/10.1002/2016sw001474

Takahashi, H., Wrasse, C. M., Figueiredo, C. A. O. B., Barros, D., Abdu, M. A., Otsuka, Y., & Shiokawa, K. (2018). Equatorial plasma bubble seeding by mstids in the ionosphere. *Progress in Earth and Planetary Science*, *5*(1), 1–13. https://doi.org/10.1186/s40645-018-0189-2

Takahashi, H., Wrasse, C. M., Otsuka, Y., Ivo, A. S., Paulino, I., Medeiros, A. F., et al. (2015). Plasma bubble monitoring by tec map and 630 nm airglow image. *Journal of Atmospheric and Solar-Terrestrial Physics*, 151–158. https://doi.org/10.1016/j.jastp.2015.06.003

Tang, L., Chen, W., Louis, O.-P., & Chen, M. (2020). Study on seasonal variations of plasma bubble occurrence over Hong Kong area using GNSS observations. *Remote Sensing*, *12*(15), 2423. https://doi.org/10.3390/rs12152423

Thampi, S. V., Yamamoto, M., Tsunoda, R. T., Otsuka, Y., Tsugawa, T., Uemoto, J., & Ishii, M. (2009). First observations of large-scale wave structure and equatorial spread f using CERTO radio beacon on the C/NOFS satellite. *Geophysical Research Letters*, *36*(18), L18111. https://doi.org/10.1029/2009gl039887

Thébault, E., Finlay, C. C., Beggan, C. D., Alken, P., Aubert, J., Barrois, O., et al. (2015). International geomagnetic reference field: The 12th generation. *Earth Planets and Space*, *67*(1), 79. https://doi.org/10.1186/s40623-015-0228-9

Tsugawa, T., Otsuka, Y., Coster, A., & Saito, A. (2007). Medium-scale traveling ionospheric disturbances detected with dense and wide tec maps over North America. *Geophysical Research Letters*, *34*(22), L22101. https://doi.org/10.1029/2007gl031663

Tsugawa, T., Shiokawa, K., Otsuka, Y., Ogawa, T., Saito, A., & Nishioka, M. (2006). Geomagnetic conjugate observations of large-scale traveling ionospheric disturbances using GPS networks in Japan and Australia. *Journal of Geophysical Research*, *111*(A2), A02302. https://doi.org/10.1029/2005ja011300

Tsunoda, R. T. (1981). Time evolution and dynamics of equatorial backscatter plumes 1. Growth phase. *Journal of Geophysical Research*, *86*(A1), 139–149. https://doi.org/10.1029/ja086ia01p00139

Tsunoda, R. T. (1985). Control of the seasonal and longitudinal occurrence of equatorial scintillations by the longitudinal gradient in integrated e region pedersen conductivity. *Journal of Geophysical Research*, *90*(A1), 447–456. https://doi.org/10.1029/ja090ia01p00447

Tsunoda, R. T. (2006). Day-to-day variability in equatorial spread F: Is there some physics missing? *Geophysical Research Letters*, *33*(16), L16106. https://doi.org/10.1029/2006gl025956

Tsunoda, R. T., Livingston, R. C., McClure, J. P., & Hanson, W. B. (1982). Equatorial plasma bubbles: Vertically elongated wedges from the bottomside F layer. *Journal of Geophysical Research*, *87*(A11), 9171–9180. https://doi.org/10.1029/ja087ia11p09171

Tulasi Ram, S., Rama Rao, P., Prasad, D., Niranjan, K., Gopi Krishna, S., Sridharan, R., & Ravindran, S. (2008). Local time dependent response of postsunset ESF during geomagnetic storms. *Journal of Geophysical Research*, *113*(A7). https://doi.org/10.1029/2007ja012922

Tulasi Ram, S., Yamamoto, M., Tsunoda, R., Chau, H., Hoang, T., Damtie, B., et al. (2014). Characteristics of large-scale wave structure observed from African and southeast Asian longitudinal sectors. *Journal of Geophysical Research: Space Physics*, *119*(3), 2288–2297. https://doi.org/10.1002/2013ja019712

Tulasi Ram, S., Yamamoto, M., Tsunoda, R., Thampi, S., & Gurubaran, S. (2012). On the application of differential phase measurements to study the zonal large scale wave structure (LSWS) in the ionospheric electron content. *Radio Science*, *47*(2). https://doi.org/10.1029/2011rs004870

Venkatesh, K., Fagundes, P., Seemala, G. K., de Jesus, R., de Abreu, A., & Pillat, V. (2014). On the performance of the iri-2012 and nequick2 models during the increasing phase of the unusual 24th solar cycle in the Brazilian equatorial and low-latitude sectors. *Journal of Geophysical Research: Space Physics*, *119*(6), 5087–5105. https://doi.org/10.1002/2014ja019960

Woodman, R. F., & LaHoz, C. (1976). Radar observations of F region equatorial irregularities. *Journal of Geophysical Research*, *81*(31), 5447–5466. https://doi.org/10.1029/ja081i031p05447

Wrasse, C. M., Figueiredo, C. A. O. B., Barros, D., Takahashi, H., Carrasco, A. J., Vital, L. F. R., et al. (2021). Interaction between equatorial plasma bubbles and a medium-scale traveling ionospheric disturbance, observed by oi 630 nm airglow imaging at bom jesus de lapa, Brazil. *Earth and Planetary Physics*, *5*(5), 1–10.

Yokoyama, T., Shinagawa, H., & Jin, H. (2014). Nonlinear growth, bifurcation, and pinching of equatorial plasma bubble simulated by three-dimensional high-resolution bubble model. *Journal of Geophysical Research: Space Physics*, *119*(12), 10–474. https://doi.org/10.1002/2014ja020708

Zalesak, S., & Huba, J. (1991). Effect of meridional winds on the development of equatorial spread F. *Eos, Transactions American Geophysical Union*, *72*, 17.

Zalesak, S., & Ossakow, S. (1980). Nonlinear equatorial spread f: Spatially large bubbles resulting from large horizontal scale initial perturbations. *Journal of Geophysical Research*, *85*(A5), 2131–2142. https://doi.org/10.1029/ja085ia05p02131